JGR Atmospheres

Superposition of Gobi Dust and Southeast Asian Biomass Burning: The Effect of Multisource Long-Range Transport on Aerosol Optical Properties and Regional Meteorology Modification

Kan Huang[1,2,3] (iD), **Joshua S. Fu**[3] (iD), **Neng-Hui Lin**[4], **Sheng-Hsiang Wang**[4], **Xinyi Dong**[3], and **Guochen Wang**[1]

[1]Center for Atmospheric Chemistry Study, Shanghai Key Laboratory of Atmospheric Particle Pollution and Prevention (LAP[3]), Department of Environmental Science and Engineering, Fudan University, Shanghai, China, [2]Shanghai Institute of Eco-Chongming (SIEC), Shanghai, China, [3]Department of Civil and Environmental Engineering, University of Tennessee, Knoxville, TN, USA, [4]Department of Atmospheric Sciences, National Central University, Taoyuan, Taiwan

Abstract One unique long-range transport event with multiple layers of aerosol plumes was observed over Taiwan during 29–31 March 2006. A synergy of ground-based observation, remote sensing, and backward trajectory simulation collectively indicated the high-altitude (above 3 km) plume originated from biomass burning in Southeast Asia while the midaltitude (around 0.8–2 km) plume was attributed to dust from the Gobi Desert. Aerosol optical properties measured at a low-altitude site were characterized of abundant coarse mode particles and increased single scattering albedo as a function of increased wavelength, indicating the influence from dust particles. While at a high mountain site (elevation of ~3 km), aerosol optical depth was elevated by a factor of 3–4 compared to its background value and mainly comprised of fine particles. It was diagnosed that the high-altitude aerosols were influenced by the transported smoke plumes but exempted from dust. Simulation of the meteorological conditions against a Taiwan-wide meteorology network showed strong near surface temperature rise of more than 2° during this long-range transport event as well as for the vertical temperature profiles. Both dust and biomass burning aerosol plumes via long-range transport contributed significantly to the atmospheric warming, resulting in strong instantaneous aerosol radiative forcing of 46.0 W/m^2 in the atmosphere. A "double dome" warming effect mechanism was proposed that both biomass burning and dust plumes above the boundary layer could efficiently reserve the solar energy and heat the lower troposphere.

1. Introduction

Even though it has been widely recognized that aerosol has undeniable effects on climate, the understanding of aerosol radiative forcing is still ambiguous. The Intergovernmental Panel on Climate Change Fifth Assessment Report summarized the best estimates of radiative forcing due to aerosol from the previous assessment reports (Myhre et al., 2013). In terms of the radiative forcing of typical aerosol components such as sulfate and black carbon, Second Assessment Report, Third Assessment Report, AR4 (Fourth Assessment Report), and AR5 (Fifth Assessment Report) showed relatively consistent results. As for biomass burning aerosol, its radiative forcing was estimated to be −0.10 (−0.30 to −0.03) W/m^2 in TAR, −0.05 (0.00 to −0.10) W/m^2 in AR4, and −0.09 (−0.16 to −0.03) W/m^2 in AR5, respectively. While for mineral dust, its radiative forcing was estimated to be −0.60 to +0.40 W/m^2 in TAR, −0.10 (−0.30 to +0.10) W/m^2 in AR4, and −0.10 (−0.30 to +0.10) W/m^2 in AR5, respectively. We can clearly see that the determined magnitudes of radiative forcing due to biomass burning and dust aerosols were still highly uncertain even the Intergovernmental Panel on Climate Change report has been periodically updating, indicating the climatic effects of these two types of aerosol are subject to a very low level of scientific understanding.

One of the commonness of dust and biomass burning aerosol is their ability to absorb the sunlight. Mineral dust has the highest absorption at the near infrared wavelengths in contrast to biomass burning and other anthropogenic aerosols, where the absorption becomes stronger in the ultraviolet solar range region (Dubovik et al., 2002). Although dust and biomass burning aerosol are both absorbing to a certain extent, their respective optical properties are distinctly different. For instance, biomass burning aerosol usually

showed very high absorption Ångström exponent (AAE) while plumes affected by dust may present negative AAE values (Loría-Salazar et al., 2014).

Dust and biomass burning aerosols were found having different climatic effects due to their different microphysical properties. Based on model simulation, strongly absorbing aerosols due to biomass burning may warm and stabilize the lower troposphere and reenforce winter-like synoptic cyclonic activities in southern Amazonia (Zhang et al., 2009). During a field campaign in the early 2000 in northeastern South Africa, the rising smoke plumes were able to penetrate the successive regional inversion layers and impacted heavily on the vertical heating rate profiles with a significant surface shortwave forcing of more than -50 W/m^2 [*James R.* Campbell et al., 2003]. In the same campaign, the radiative effects of biomass aerosol at top of the atmosphere could be significantly changed from negative values of -13.0 W/m^2 in clear skies to positive values of $+11.5$ W/m^2 in the presence of clouds (Keil & Haywood, 2003). Similarly, based on aircraft soundings in the vicinity of the California coast, the heating rate in the biomass burning layer could be enhanced ($+0.8$ K/day) under the presence of clouds (Mardi et al., 2018). In the Yangtze River Delta region of China, Ding et al. (2013) demonstrated an observation-based air pollution-weather interaction from an intense air pollution event from mixed agricultural burning plumes with fossil fuel combustion. Surface temperature was decreased by up to 10 K (Kelvin) and precipitation was significantly suppressed due to severe air pollution. As for Southeast Asia, the transported smoke plumes from this region enhanced the free tropospheric warming over the northern South China Sea (Pani et al., 2016). The water-soluble components and black carbon in the biomass burning plumes were the main contributors to the aerosol radiative forcing. The heating rates due to black carbon were higher than those due to the total aerosols. In a case study of two-layer heavy smoke long-range transport, enhanced aerosol radiative efficiency at both surface and lower atmosphere were found with high atmospheric heating rate of 1.3 K/day ([Pani et al., 2016).

As for dust, Noh et al. (2012) showed that dust particles had negligible effects on radiative heating. However, Won et al. (2004) found contrasted results that the elevated dust layer may have an intrinsic self-sustaining mechanism, making the dust layer more stable. On a larger scale, mineral aerosols were found related to cloud properties over North Africa and the North Atlantic, exhibiting suppressing effect on precipitation in thin low altitude clouds and changing cloud amounts in ice phase clouds (Mahowald & Kiehl, 2003). In the framework of Aerosol Robotic Network (AERONET), the mixed dust-anthropogenic aerosols exhibited higher warming efficiency in the atmosphere than either anthropogenic or dust aerosols (Tian, Zhang, Ma, et al., 2018; Tian, Zhang, Cao, et al., 2018).

In regard of the inadequate understanding of dust and biomass burning aerosols, the mixing of these two types of aerosols would make the physicochemical properties of the mixture more complicated and the resulted climatic effects more unpredictable. Most studies on the mixing of dust and biomass burning aerosols focused on Africa where dust and biomass burning emissions were both intensive. An individual particle analysis showed efficient internally mixing of biomass burning and Saharan dust particles (Hand et al., 2010), which would change the optical properties of ensemble particles. There was a number of studies using the remote sensing technique such as lidar and Sun photometer. Combination of the particle linear depolarization ratio and the lidar ratio at two wavelengths allowed a classification of the aerosol types, including marine aerosol, Saharan dust, and a mixture of dust-biomass burning (Groß et al., 2011). In the framework of the Saharan Mineral Dust Experiment, multiple events of elevated biomass burning layer above dust were detected and it was found that that all biomass burning aerosol layers contained a varying fraction of large dust particles. The fraction of dust followed the increase of the effective diameter and the absorption Ångström exponent (Weinzierl et al., 2011). Comparison of three Saharan Mineral Dust Experiment campaigns (two in summer with dust only and one in winter with additional biomass burning) summarized a variety of parameters for distinguishing dust, smoke, and mixture of dust and smoke based on multiwavelength polarization Raman lidar observation, including aerosol layer top height, lidar ratio, depolarization ratio, and absorption Ångström exponent (Tesche et al., 2011). A shipborne lidar observation from the Caribbean to western Africa observed decrease of lidar ratio in the Sahara dust layer with the contribution from fire smoke particles (Rittmeister et al., 2017). In another shipborne lidar study, the radiative effects of aerosols above the northern and southern Atlantic Ocean were estimated. The microphysical parameters and mixing fraction of aerosol types were assumed for radiative transfer calculation during a mixed

dust/smoke event over the ocean (Kanitz et al., 2013). Similarly, an airborne high-resolution lidar measurement of Saharan dust, partly mixed with biomass-burning smoke also assumed single scattering albedo and the asymmetry parameter, causing high uncertainties in the calculation of aerosol solar radiative forcing (Bauer et al., 2011). Sicard et al. (2012) captured a concurrence episode of intense dust and extremely fresh biomass burning from Africa. It was found that the mixed dust particles exhibited even stronger absorption than smoke based on the single scattering albedo. Strong shortwave heating rate of 2–3 K/day was calculated for both dust and smoke aerosols. In another interesting study during the ex-hurricane Ophelia on 15–16 October 2017, dust from the Sahara and smoke from Portuguese forest fires were brought to the British Isles, causing an unprecedented high aerosol optical depth (AOD) and estimated peak concentrations of $420 \pm 200 \ \mu/gm^3$ for the dust and $558 \pm 232 \ \mu/gm^3$ for the biomass burning aerosols, respectively (Osborne et al., 2019).

In Asia, dust and biomass burning events were generally separately studied and the mixing between these two aerosol types were rarely investigated (Huang et al., 2010; Nguyen et al., 2015). In this study, a long-range transport episode with participation of both dust and biomass burning was observed over Taiwan. The goal of this work is to elucidate the influence of aerosols on the perturbation of regional meteorology. The spring in 2006 was a season with both strong dust storms from the Gobi Desert (Chang et al., 2010; Kim et al., 2008; Wang et al., 2008) and intense biomass burning activities in Southeast Asia (Fu et al., 2012). Thus, it was a good timing for studying the long-range transport impact of concurrent dust and biomass burning aerosols. The structure of this paper is organized as follows. Section 2 describes the applied measurement instruments and methodologies. In section 3, the sources of the decoupled aerosol plumes were diagnosed. Then different aerosol optical properties of the plumes were analyzed by taking the advantage of monitoring at ground and high mountain sites. In section 4, the warming effect due to the intruded aerosol plumes was unveiled based on both 3-D numerical simulation and radiative transfer modeling. Concluding remarks are given in section 5.

2. Methodology

2.1. Observations

2.1.1. MicroPulse Lidar Observation

Aerosol vertical profiles were retrieved by a MicroPulse Lidar (MPL) located in the National Central University (NCU) north of Taiwan (Fig. 1c). The EPA-NCU MPL system is maintained by Taiwan Environmental Protection Administration and joined the NASA MPLNET network (http://mplnet.gsfc. nasa.gov/) since 2005. The MPL is a compact and eye-safe elastic backscatter lidar system at a single wavelength of 527 nm. Briefly, MPL fires a short pulse of laser light into the atmosphere and measures the returned backscattered signal. The instrument calibrations, an algorithm for processing the normalized relative backscatter product (NRB; the relative signal strength of backscatter), and associated uncertainties can be referred by Welton et al. (2002) and Campbell et al. (2002). The vertical resolution of the MPL measurement is 75 m.

2.1.2. AERONET Observation

Identification of the dominant aerosol types and mixtures is possible based on the relationship among some key aerosol optical parameters, for example, single scattering albedo, extinction/absorption Ångström exponent, and fine mode aerosol fraction (Giles et al., 2012). In this study, aerosol optical properties were collected from the AERONET by using the CIMEL sun-sky photometer (Holben et al., 1998). Various parameters of aerosol optical properties for the whole atmospheric column were retrieved at the wavelength of 440, 670, 870, and 1,020 nm. The Ångström exponent, single scattering albedo, aerosol size distribution, and refractive index can be retrieved by using sky radiance almucantar measurements and direct sun measurements (Dubovik et al., 2002).

AOD represents the extinction of solar radiation due to aerosols and could be regarded as one of the parameters representing aerosol burden in the atmospheric column. AOD less than 0.1 could be regarded as clean while AOD higher than 1.0 are regarded as highly polluted. Ångström exponent (α) is a parameter that can reflect the aerosol sizes. $\alpha > 1$ indicates the dominance of fine particles mainly from anthropogenic sources such as BC or sulfate, while $\alpha < 1$ indicates the dominance of coarse particles such as mineral dust and sea salt (Eck et al., 1999; Foyo-Moreno et al., 2019). Single scattering albedo (SSA) is defined as the ratio of scattering to the total extinction (scattering and absorption). As for purely scattering aerosols such as

sulfate and nitrate, SSA is close to 1.0. While strongly absorbing aerosols (i.e., soot/black carbon) have much lower SSA of less than 0.5 at a wide spectrum range (Wang et al., 2007).

The AERONET sites used in this study included two sites in mainland China (Fig. 3f), for example, Xianghe (39°45′N, 116°58′E, meters above sea level: 36 m) and Taihu (31°25′N, 120°13′E, 20 m), and two sites in Taiwan (Fig. 4a), that is, Taipei-CWB (25°1′N, 121°30′E, 26 m), and one background high mountain site, Lulin (23°28′N, 120°52′E, 2,868 m).

2.1.3. Auxiliary Data

PM_{10} concentrations (based on the beta attenuation principle) in 86 Chinese cities were derived from air pollution index via the data center of Ministry of Environmental Protection of China (http://datacenter.mee.gov. cn/websjzx/dataproduct/resourceproduct/queryResourceList.vm?rocde=). Conversion from air pollution index to PM_{10} was explicitly described in Wang et al. (2018). In addition, PM_{10} concentrations in some other Asian countries can be obtained via various sources. The data of Korea can be obtained from the Korean Meteorological Administration (http://www.kma.go.kr/eng/weather/asiandust/timeseries.jsp). The data of Thailand can be obtained from its Pollution Control Department (http://air4thai.pcd.go.th/webV2/index. php), and the air quality data of Japan used in this study are archived by EANET (The Acid Deposition Monitoring Network in East Asia, https://www.eanet.asia/) upon request. Ultraviolet Aerosol Index (UVAI) was retrieved from Ozone Monitoring Instrument. Ground-based meteorology data of Taiwan were from Taiwan's Environmental Protection Administration (http://www.epa.gov.tw). Meteorological sounding data on UTC time of 0:00 and 12:00 at selected sites were available from http://weather.uwyo.edu/upper-air/sounding.html website.

2.2. Simulation of Meteorological Conditions

Simulation of meteorological conditions was performed by the Weather Research and Forecasting (WRF) model v3.4. The final analyses data set (ds083.2) with a horizontal resolution of 1.0° × 1.0° and a temporal resolution of 6 hr from National Centers for Environmental Prediction was digested into WRF as initial and boundary conditions. Key module settings in WRF were summarized as follows: precipitation (WRF single-moment 3-class scheme), longwave radiation (RRTM), shortwave radiation (Dudhia scheme), surface-layer option (MM5 similarity; Monin-Obukhov scheme), advection (Global mass-conserving scheme), planetary boundary layer scheme (YSU), and cumulus option (Grell). This set of parameterization schemes had been applied for the East and Southeast Asia domain (Fu et al., 2012; Huang et al., 2013). The model vertical layers extended from the surface to 50 mb with 34 vertical layers. The horizontal grid resolution of WRF was set as 36 × 36 km in this study. The modeling domain is shown in Figure S1 in the supporting information.

To evaluate the model performance of the WRF simulation, the grid cell was first identified based on the longitude and latitude of each meteorology station in Taiwan. Then the values of observation and simulation were averaged at each time step and at all the extracted grid cells for comparison. The time difference between local time in Taiwan and model is 8 hr.

The air mass backward trajectory was simulated using the Hybrid Single Particle Lagrangian Integrated Trajectory Model. It was run online at the National Oceanic and Atmospheric Administration Air Resource Laboratory READY website (https://ready.arl.noaa.gov/HYSPLIT_traj.php). The meteorological input data used in the model was obtained from National Centers for Environmental Prediction's global data assimilation system with a horizontal resolution of 1° × 1° and a time resolution of 3 hr.

2.3. Simulation of Aerosol Heating Rates and Radiative Forcing

Atmospheric heating rates and radiative forcing due to aerosols in the atmosphere were calculated by using a solar radiative transfer model (CLIRAD-SW) developed by Chou and Suarez (1999) and Chou et al. (2002). This model considered solar radiation absorption by water vapor, O_3, O_2, CO_2, Rayleigh scattering, and the absorption and scattering due to aerosols. Fomin and Correa (2005) implemented new parameterizations in CLIRAD-SW and the version used in this study was called CLIRAD (FC05)-SW. Vertical profiles of the aerosol optical parameters are required as inputs for the radiative transfer model. The vertical resolution is set as 225 m (3 times of the vertical resolution of the MPL measurement) and the calculation of aerosol radiative forcing covered altitudes from the surface to around 7 km.

Spectrum of aerosol was divided into eight bands from 200 to 10,000 nm in the model. The input parameters for calculating the aerosol radiative forcing and heating rates included wavelength dependent AOD (i.e., including both scattering and absorption), single scattering albedo, and asymmetry factor. Since the AERONET inversions (level 2.0) are only available at the wavelength of 440–1,020 nm, aerosol microphysical properties at the other wavelengths are needed to be interpolated. As for the interpolation of AOD, the Ångström exponent (AE) of total aerosol can be calculated via

$$AE_{440-1020} = -\ln(AOD_{440}/AOD_{1020})/\ln(440/1020), \tag{1}$$

Then AOD at different wavelengths can be obtained

$$AOD_\lambda = \exp(-AE_{440-1020} \times \ln(\lambda/\lambda_{ref}))*AOD_{ref}, \tag{2}$$

where λ is the wavelength that the aerosol optical properties are to be interpolated. λ_{ref} is 527 nm that the MPL lidar operated on. To obtain single scattering albedo at different wavelengths, the AAE was first derived via

$$AAE_{440-1020} = -\ln(AAOD_{440}/AAOD_{1020})/\ln(440/1020), \tag{3}$$

Then AAOD at all wavelengths can be derived as similar as the interpolation of AOD above. Finally, the single scattering albedo at all wavelengths can be calculated via

$$SSA_\lambda = 1 - AAOD_\lambda/AOD_\lambda, \tag{4}$$

As for the asymmetry factor at other wavelengths, it was derived based on the fitted power function regression curve from the AERONET inversion. In section 3.3.3, the real inputs for the model were described in more details. The surface albedo for this study period was derived from the Moderate Resolution Imaging Spectroradiometer 16-day Albedo products (MCD43C3.005). The atmospheric heating rates can be calculated using the equation below:

$$\frac{\partial T}{\partial t} = \frac{g_a}{C_p} = \frac{\Delta F(p)}{\Delta p}, \tag{5}$$

where $\frac{\partial T}{\partial t}$ is the heating rate (K/day), g_a is the acceleration due to gravity, c_p is the specific heat capacity of air at constant pressure ($\sim$1,006 J kg^{-1} K^{-1}) and $\Delta F(p)$ is the net flux divergence of a pressure layer p.

The atmospheric heating rate (HR) due to aerosols is then given by the equation below:

$$HR = \frac{\partial T}{\partial t} \text{ (with aerosols)} - \frac{\partial T}{\partial t} \quad \text{(without aerosols)}, \tag{6}$$

To derive the atmospheric heating rates and radiative forcing solely due to aerosols in the atmosphere, the simulation by inputting the required aerosol optical parameters was firstly conducted. Then a sensitivity simulation without aerosols was conducted by setting the AOD values as zero at all altitudes. Finally, the differences between the two simulations can derive the radiative forcing and heating rate solely due to aerosols.

3. Results

3.1. Detection of Multilayered Aerosol Plumes From Contrasted Source Regions

3.1.1. Process Analysis of a Long-Range Transport Event

On 29–31 March 2006, one notable particulate pollution event was detected by the EPA-NCU MPL site in Taiwan. Figure 1a displays the time-height cross section of the NRB retrieved from the MPL. On the first half day of 29 March, aerosol was mainly confined below the cloud base around 2 km. The NRB signal was almost absent above this height, indicating negligible intruded emissions. Starting at around 11 UTC, an evident aerosol plume commenced at altitudes around 3.7–4.4 km. This thick plume (width of ~1 km) lasted more than 34 hr till 21 UTC on 30 March. The top height of the plume gradually decreased as a function of time.
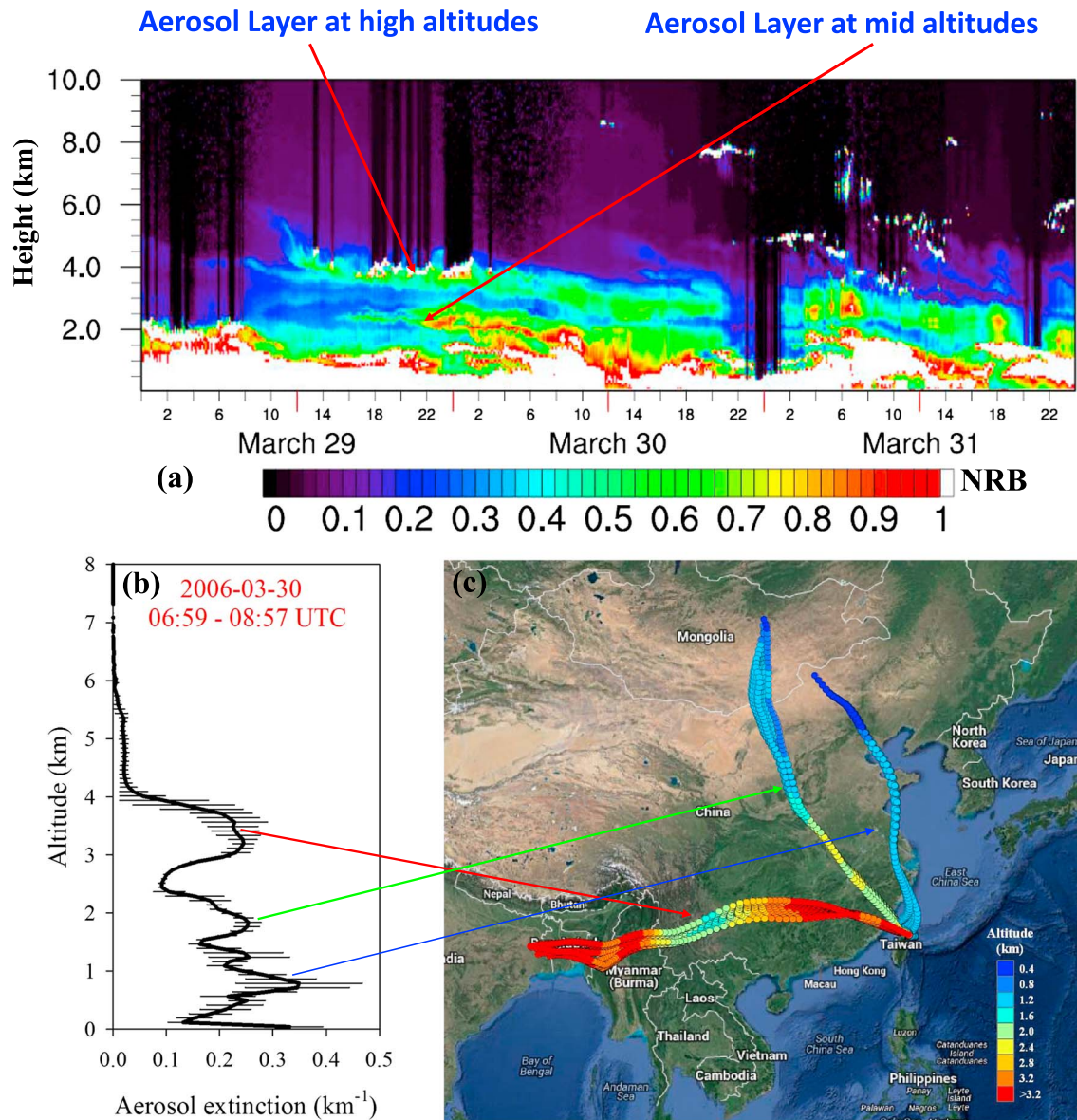
Figure 1. (a) MPL NRB (normalized relative backscatter, unit: counts*km²/µj*µs) at 527 nm from 29 to 31 March 2006 (Date and time are presented in the form of UTC) at the EPA-NCU site. (b) MPL-derived aerosol extinction profiles averaged for 06: 59–8: 57 UTC on 30 March. The bars represent one standard deviation. (c) The 72-hr backward air mass trajectories starting at the NCU MPL site at three levels of 0.8, 1.9, and 3.5 km corresponding to the altitudes of the observed extinction peaks in Figure 1b. NRB = normalized relative backscatter; MPL = MicroPulse Lidar.

However, the bottom height of the plume still remained at relatively high altitudes of above 2 km, indicating a strong invaded source from nonlocal emissions.

What was interesting and unique about this episode was that about 3 hr after the appearance of the plume referred above, another plume penetrated between the upper layer aerosol plume and the near-surface aerosol layer as shown in Figure 1a. In the early stage from 15 to 20 UTC on 29 March, only a slim aerosol plume was detected in the middle layer. After 20 UTC, this plume expanded with thickness of more than 1 km. The NRB data illustrated that the denser part of aerosol plume in the middle layer lasted about 12 hr from 22 UTC on 29 March to 10 UTC on 30 March. At the same time, this plume descended with height and tended to gradually mix into the boundary layer. This was clearly observed after 16 UTC on 30 March, the dense aerosol stripe in the middle layer almost dissipated but mixed more homogeneously as indicated by the

NRB signal between 16 and 21 UTC. Overall, there was a clear delineation of the upper and middle aerosol layers from 29 to 30 March while the middle aerosol layer tended to gradually merge into the boundary layer. From around 21 UTC on 30 March to 1 UTC on 31 March, a clear interception of both plumes was indicated by the NRB data. This was due to the precipitation along the east and south coasts of China as observed from the Tropical Rainfall Measuring Mission satellite (Figure S2). After that, these two aerosol plumes commenced again, suggesting a continuous long-range transport from elsewhere. From 3 UTC on 31 March, the two plumes began to mix together, which would surely modify the physiochemical properties of transported aerosols.

3.1.2. Identification of Source Regions for Multilayered Aerosol Plumes

Vertical profiles of aerosol total extinction between 06: 59 and 8: 57 UTC on 30 March were retrieved and the average profile is shown in Figure 1b, with error bars representing one standard deviation. As expected, multiple peaks showed at different altitudes, different from most previous studies that aerosol extinction usually decreased with altitudes when local emissions dominated [Huang et al., 2012; S H Wang et al., 2010]. Near the ground level, aerosol extinction anomalously increased with altitudes and peaked at around 0.7–0.8 km with the mean value of 0.35 ± 0.11 km^{-1}. At altitudes between 0.8 and 2.5 km, although the aerosol extinction exhibited an overall decreasing trend with altitudes, two pronounced peaks were observed at around 1.3 and 1.8 km, with values of 0.25 ± 0.075 and 0.25 ± 0.022 km^{-1}, respectively. Above 2.5 km, the aerosol extinction started to gradually increase again with altitudes and reached another peak at a much higher altitude of around 3.3 km. Different from the peaks observed at the lower and middle levels, the aerosol plume in the upper layer with high extinctions was evidently much thicker extending from 2.9 to 3.7 km. Mean aerosol extinction within this altitude reached 0.23 ± 0.038 km^{-1}, which was at the similar magnitude as those peaks observed at the lower and middle altitudes.

To diagnose the potential source regions of the aerosol plumes at different altitudes as discussed above, 72-hr backward air mass trajectories at the MPL site were simulated by the Hybrid Single Particle Lagrangian Integrated Trajectory model (Draxier & Hess, 1998; Draxler & Rolph, 2015). Backward trajectories starting at UTC 08:00 on 30 March were computed at three levels of 0.8, 1.9, and 3.5 km (Figure 1c), corresponding to the altitudes of the observed extinction peaks (see the link lines between Figures 1b and 1c). It was evident that the backward trajectories at the lower and middle altitudes of 0.8 and 1.9 km both traced back to the arid and semiarid regions in inner-Mongolia of China and Mongolia where the Gobi Desert is located. Spring is the season when Asian dust storms frequently outbroke and 2006 was a strong dust storm year, which had been documented in previous studies [Huang, Zhuang, Lin, et al., 2010; Papayannis et al., 2007; W Wang et al., 2008]. A climatology study of Asian dusts that passed over Taiwan in 2004 and 2005 found that the dust layers usually resided at altitudes of 1–4 km (Chen et al., 2007). Thus, the aerosol plumes observed at the low and middle altitudes were evidently characterized of mineral dust origin. Figure S3 depicts the spatiotemporal evolution of daily PM$_{10}$ concentrations over mainland China, Korea and Japan during 27–30 March 2006. As visualized by the circles denoting the heavily polluted areas, on 27 and 28 March, a considerable number of cities in the northern China exceeded PM$_{10}$ concentrations of 200 μg/m^3, further spreading over South Korea and part of Japan. On the following 2 days of 29 and 30 March, heavy pollution drifted toward the eastern and southern China, causing elevated PM$_{10}$ concentrations about 2–3 times of the previous 2 days. A clear transport pathway could be visualized as from the northern China toward the east and south coasts, which was one of the typical transport pathways of the spring dust storm originating from the Gobi Desert [F Tsai et al., 2008].

In contrast, backward trajectories starting at 3.5 km traced back to the Indo-China Peninsula in Southeast Asia, mainly from Myanmar. It is noted that the air mass trajectories originating from Myanmar remained at high altitudes of above 3 km, far exceeding the height of boundary layer, thus precluding the possibility from local anthropogenic emissions in Southeast Asia. A strongly seasonal dependent emission source in Southeast Asia was biomass burning with strongest fire activities during the premonsoon dry season, generally from February to April (Tsay et al., 2013). Figure S3 overlays the spatial distribution of Fire Locating and Modeling of Burning Emissions biomass burning carbon emissions (Reid et al., 2009) on a daily basis. Hot spots were evident in the Indo-China Peninsula, spreading over Myanmar, northern part of Laos, and Thailand. Biomass burning activities were most active on 27 and 28 March. Due to the presence of mountain ranges at the east and west coast of the Southeast Asia peninsula, winds below 850 hPa were channeled toward the north while only when biomass burning plumes were lifted to a threshold height, it can be
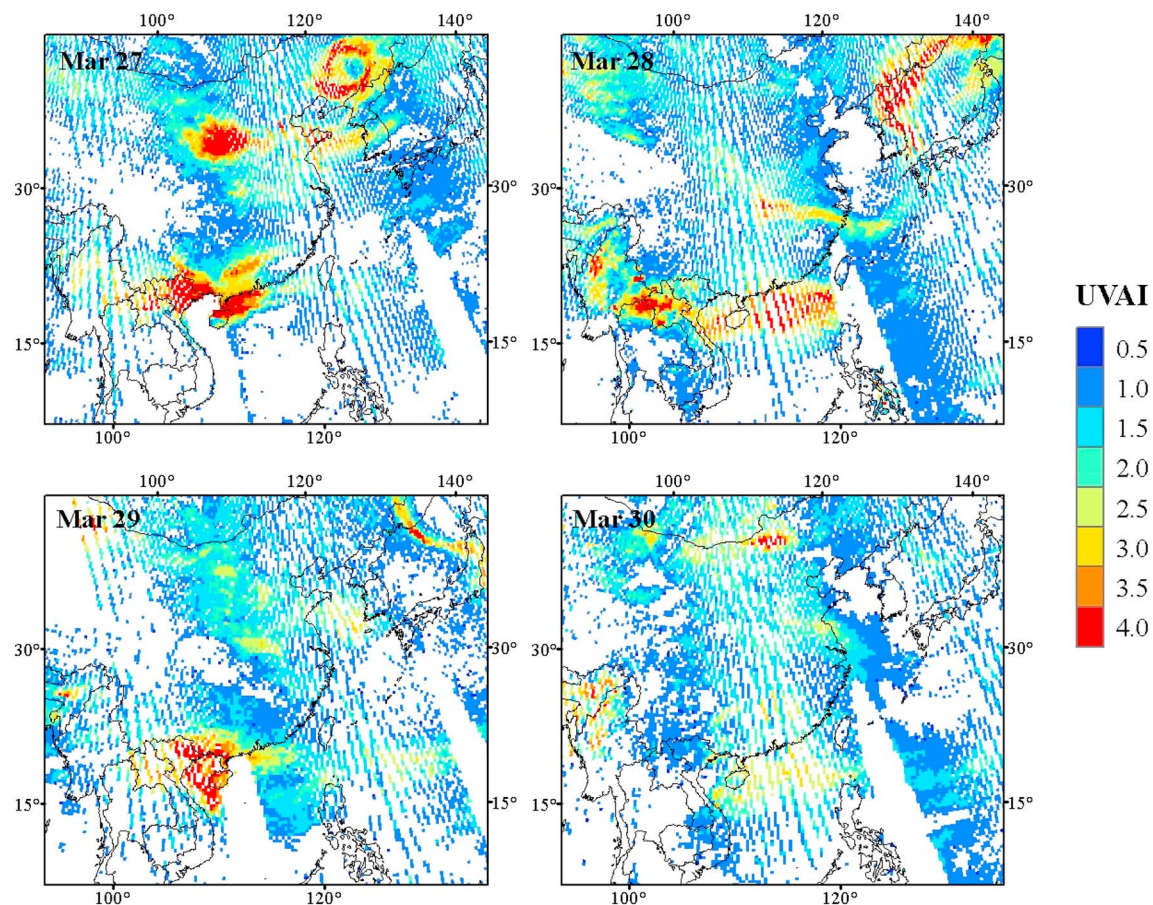
Figure 2. Spatiotemporal evolution of UVAI retrieved from Ozone Monitoring Instrument during 27–30 March 2006. UVAI = Ultraviolet Aerosol Index.

transported eastward driven by the winter tropical Southeast Asian High (Lin et al., 2013). Climatology study showed that the enhancement of the local East-West cell/circulation by a well-organized convergent center over Indo-China at 925 hPa. in March allows the uplift of biomass burning emissions to the free troposphere (Yen et al., 2013). Figure S1 shows the mean wind fields during 27–30 March simulated by WRF and it shows strong westerlies above 1.8 km, which was consistent with the backward trajectory analysis. Overall, all the evidences provided above indicated the upper layer aerosol plume derived from the biomass burning source region in Southeast Asia.

Figure 2 further depicts the transport behavior of the aerosol plumes from the perspective of remote sensing. UVAI retrieved from Ozone Monitoring Instrument is a parameter sensitive to the absorbing aerosol (Torres et al., 2007), for example, biomass burning aerosol with enriched black carbon, and mineral dust in which the iron oxides minerals (hematite and goethite) had pronounced absorbance at the visible spectrum (Arimoto et al., 2002; Deaton & Balsam, 1991). Figure 2 shows higher UVAI values in both the Gobi Desert and the northern Southeast Asia peninsular. In addition, two transport routes as similar as the backward trajectories (Figure 1c) were reflected from the spatiotemporal variation of UVAI and eventually intersected over the South China Sea, further corroborating the different source regions of the aerosol plumes observed by Lidar at various altitudes.

3.2. Explicit Aerosol Microphysical Optical Properties
3.2.1. Evolution of Aerosol Optical Properties Along the Dust Transport Pathway

During the long-range transport of Asian dust, the properties of dust should be modified due to the passing over vast populous and industrialized areas of the eastern China as well as changes of environmental conditions toward the south (e.g., higher temperature and humidity; Huang et al., 2010; Pan et al., 2017; Tobo
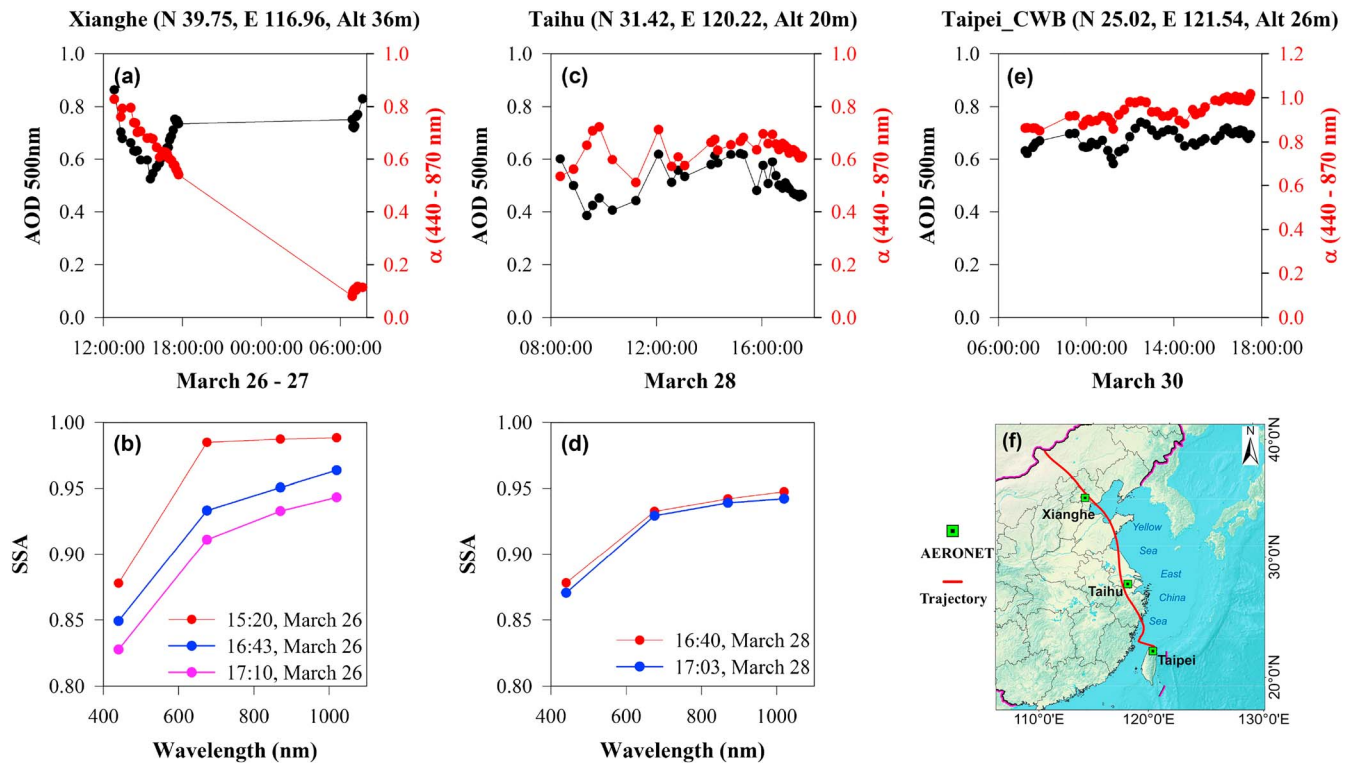
Figure 3. (a, c, and e) Time series of AOD at 500 nm and Ångström exponent (440–870 nm) at three AERONET sites (Xianghe, Taihu, and Taipei_CWB) on the dust days. (b, d) The dependence of single scattering albedo on wavelengths at Xianghe and Taihu. No inversion data of almucantar measurements were available at Taipei_CWB. (f) The 72-hr backward air mass trajectories starting at 08 UTC, 30 March 2006 and the height of 0.8 km at the NCU MPL site. The locations of three AERONET sites are marked in the figure. AOD = aerosol optical depth; AERONET = Aerosol Robotic Network.

et al., 2010). As shown in Figure 3f, two AERONET sites (i.e., Xianghe in the North China Plain and Taihu in the Yangtze River Delta) located near the dust transport pathway. Based on the simulation of backward trajectory, the air masses arriving at Taiwan on 30 March were traced back to the North China Plain on 26–27 March. As shown in Figure 3a, AOD at 500 nm (τ_{500}) ranged from 0.53 to 0.86 with a mean value of 0.66 on 26 March. Ångström exponent at 440–870 nm ($\alpha_{440-870}$) at all hours were lower than 1.0, indicating the existence of considerable coarse particles. On 27 March, τ_{500} maintained at high levels with a mean value of 0.75. At the same time, $\alpha_{440-870}$ dropped to extremely low values of 0.08–0.12, suggesting massive inputs of mineral dust. Compared to $\alpha_{440-870}$ of around 0.49 during a strong Asian dust event [Y. M. Noh et al., 2012], $\alpha_{440-870}$ at Xianghe was even lower, suggesting the presence of relatively pure dust particles. As for the almucantar inversion on 26 March (Figure 3b), SSA showed low values of less than 0.9 at 440 nm and then increased as wavelength increased. This was a typical SSA pattern of dust as the mineral components (mainly iron oxides) in dust were strongly absorptive at the ultraviolet wavelength.

After 1 day, the air masses travelled toward the Yangtze River Delta region on 28 March. The AERONET Taihu site at the conjunction of southern Jiangsu province and northern Zhejiang province is a background site. As shown in Figure 3c, τ_{500} was also high with the mean value of 0.51. Compared to 27 March at Xianghe, $\alpha_{440-870}$ at Taihu increased to a range of 0.51–0.72 but still much lower than 1.0, indicating the continuous effect of long-range transported dust. The dependence of SSA on wavelength at Taihu was as similar as Xianghe although the aerosol there tended to be more absorptive, which should be ascribed to the less scattering aerosols over the background site.

At the receptor site, that is, the AERONET Taipei-CWB site, its τ_{500} mean on March 30 reached 0.68, even higher than the upstream Taihu site and only slightly lower than the Xianghe site. In addition to the contribution from dust to AOD, the intruded biomass burning plumes also contributed to the columnar AOD, thus resulting in high AOD at the Taipei-CWB site. $\alpha_{440-870}$ at Taipei-CWB was the highest among the three sites
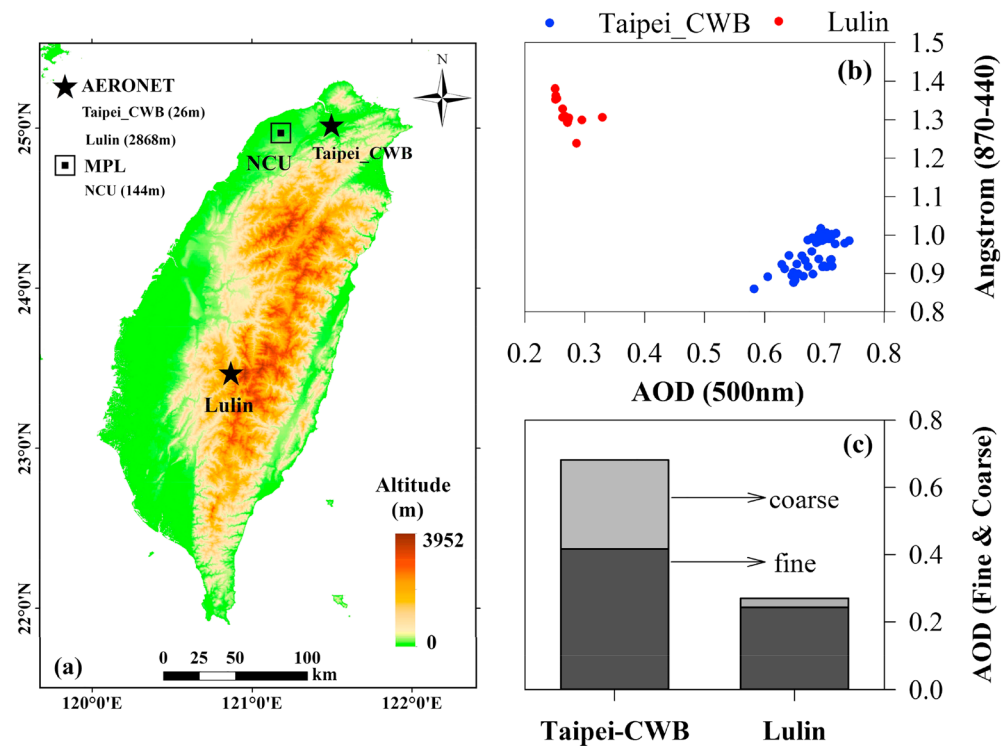
Figure 4. (a) Locations of two AERONET sites (denoted by the black stars) in Taiwan. Taipei-CWB is a near sea level site with an altitude of 26 m. Lulin is a high mountain site with an altitude of 2,868 m as visualized by the contour of terrain elevations in the figure. The EPA-NCU MPL site (denoted by the black square) is also marked in the figure. (b) Scatter plot of AOD at 500 nm versus its corresponding Angström exponent (α) at 440–870 nm at Taipei-CWB and Lulin (c) Average fine and coarse mode AOD at Taipei-CWB (23:13 UTC on 29 March to 9:29 UTC on 30 March) and Lulin (8:15–9:31 UTC on 30 March). AOD = aerosol optical depth; AERONET = Aerosol Robotic Network.

in the range of 0.86–1.02. This should be partly due to the mixing of anthropogenic particles and dust during the long-range transport passing over the industrialized and populous areas in China [Huang, Zhuang, Li, et al., 2010; *Y* Wang et al., 2005]. In addition, local fine particles over Taiwan and biomass burning aerosols in the upper layer also increased the values of $\alpha_{440-870}$. As no almucantar inversion data were available on 30 March, the spectral dependence of SSA at Taipei-CWB was not discussed here.

3.2.2. Differentiating Aerosol Optical Properties at Low and High Altitudes

There are two AERONET sites that were available for further analysis of aerosol optical properties at different altitudes in Taiwan. As shown in Figure 4a, one site is located near the ground level (Taipei-CWB: 26-m above mean sea level) and the other one is located at Mount Lulin (2,868-m above mean sea level). Height disparity of these two sites greatly facilitated the comparison of the invaded aerosol plumes at different altitudes in this study. Figure 4b shows the scatter plot of τ_{500} versus its corresponding $\alpha_{440-870}$ during the episode. Aerosol properties at the high- and low-altitude sites were distinctly differentiated. At the Taipei-CWB site, τ_{500} showed moderate/high values while $\alpha_{440-870}$ were relatively low and this phenomenon had been discussed in the previous section. Figure 4c shows the mean fine and coarse τ_{500} of 0.41 and 0.26 at Taipei-CWB (23:13 UTC on 29 March to 9:29 UTC on 30 March), respectively. The fraction of coarse mode τ_{500} to the total τ_{500} reached 39%.

At the high-altitude Mount Lulin background site (Sheu et al., 2010), τ_{500} averaged 0.27 ± 0.02 (8:15–9:31 UTC on 30 March). Although much lower than the ground site, τ_{500} at Lulin was significantly higher than its annual value of 0.07 [*S H* Wang et al., 2014], corroborating the intensive impact of the upper layer plume on this high mountain site. One multiyear (2003–2009) study also observed that PM$_{2.5}$ concentrations along with its chemical species (e.g., K$^+$, SO$_4^{2-}$, and NO$_3^-$) were the highest in March due to the transport of Southeast Asia smoke (Lee et al., 2011). Compared to the ground site, $\alpha_{440-870}$ at Lulin were much higher in the range of 1.24–1.38, indicating the dominance of fine mode particles. Figure 4c shows the mean fine
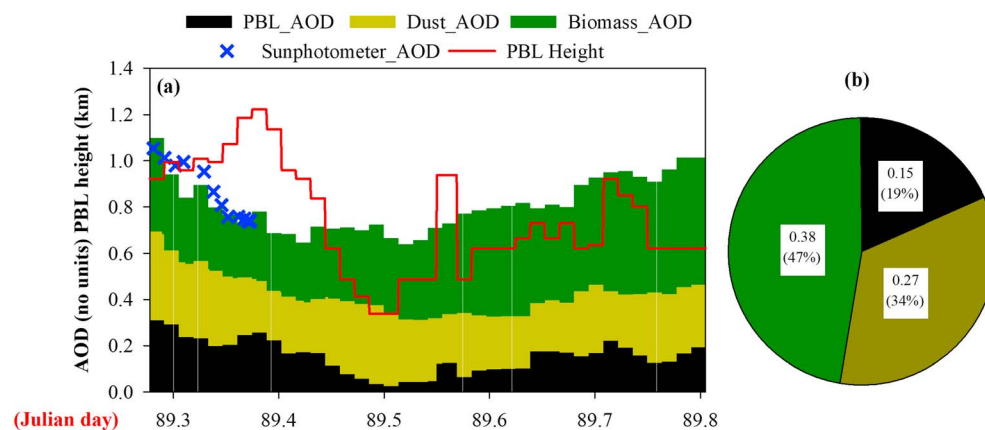
Figure 5. (a) Time series of integrated AOD within the three layers (i.e., the PBL layer, dust layer, and biomass burning layer) during a period from 2 to 19 UTC on 30 March (b) Contributions of PBL AOD, dust AOD, and biomass burning AOD to the total AOD. AOD = aerosol optical depth.

and coarse τ_{500} of 0.24 and 0.03, resulting in a low contribution of coarse mode τ_{500} to the total τ_{500} of around 10%. Hence, it implied that Lulin was almost exempt from the dust invasion. During the same period above, the MPL NRB signal (Figure 1a) showed that the upper height of the dust layer was around 2.4 km. During the whole study period, the maximum upper height of the dust layer was around 2.9 km (from 23 UTC on 29 March to 2 UTC on 30 March). As the Lulin site is located above 2.8 km, this indicated the results from MPL and AERONET were quite consistent.

3.2.3. Extent of Long-Range Transport

The whole aerosol column can be separated into three stratified layers based on the discussions above, that is, the boundary layer which trapped the majority of local anthropogenic emissions (hereinafter called the PBL layer), the dust layer, and the biomass burning layer. We chose a period from 2 to 19 UTC on 30 March when continuous aerosol extinction profiles were available from MPL. As visualized in Fig. 1a, the aerosol plumes from different sources decoupled. Thus, it was feasible to determine the top and bottom heights of each layer at each time step according to the extinction coefficient profile where it sharply decreased or increased (Noh et al., 2007). Figure 5a shows the time series of integrated AOD within the three layers. AOD within the PBL layer showed a decreasing trend from 0.31 at 7 UTC to 0.03 at 12 UTC on 30 March. It was noted that no peak values of AOD were observed during the local rush hours (usually around 9–12 UTC). During the same period, AOD within the dust layer maintained at relatively high levels of over 0.2 and increased from 0.21 on 9 UTC to 0.34 on 12 UTC. The opposite trend between the PBL AOD and dust AOD probably suggested the dilution effect of dust on the local anthropogenic aerosols. This phenomenon has been frequently observed in Taiwan, mainland China, and elsewhere (Chuang et al., 2008; Wang et al., 2018). After 12 UTC, AOD within the PBL gradually increased, likely due to the shallow boundary layer at night. Compared to the temporal variation of PBL AOD, dust AOD fluctuated less strongly, suggesting a continuous and relatively stable input of dust particles. As for AOD within the biomass burning layer, it showed an evidently increasing trend from its minimum of 0.23 at 9 UTC to the peak value of 0.56 at 19UTC. A variety of factors could be responsible for this, for example, the strengthening of Southeast Asia biomass burning emissions, variable meteorological conditions in the free troposphere, and aging of certain aerosol components.

Overall, biomass burning AOD averaged 0.38, contributing the largest fraction of 47% to the total AOD (Figure 5b). Dust AOD averaged 0.27, also contributing a considerable fraction of 34% while PBL AOD was the least of 0.15 with the contribution of 19%. In other words, AOD from non-local sources was more than 3 times than that from local sources during this long-range transport event.

4. Discussions

4.1. Regional Meteorological Impacts: Warming Effect

4.1.1. Warming Near the Surface

It would be interesting to investigate what extent the intrusion of overwhelming nonlocal aerosols could influence/modify and feedback to the regional climate since biomass burning aerosol and dust aerosol are
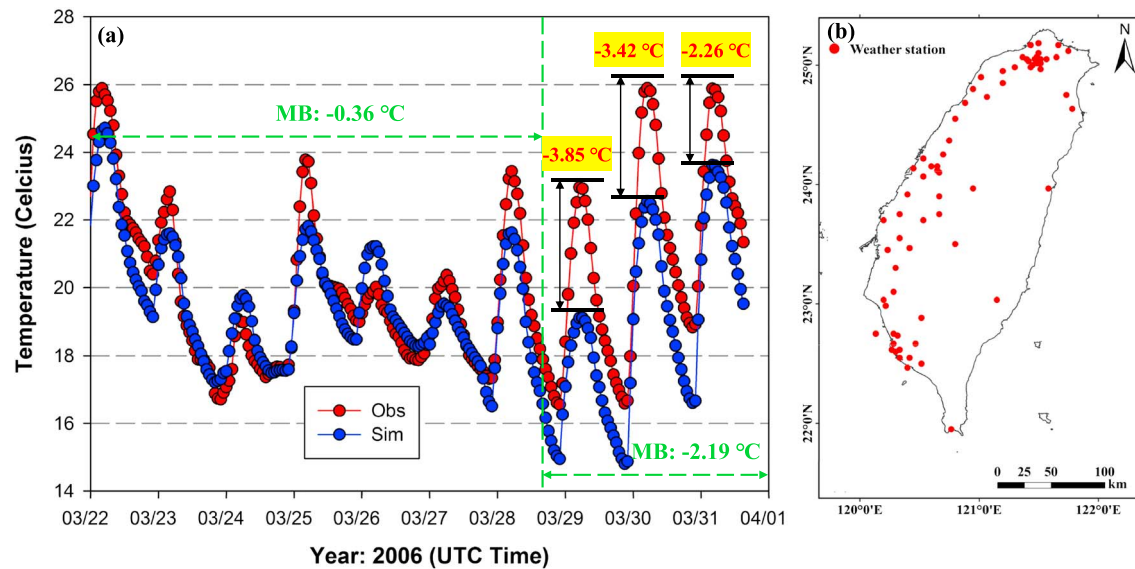
Figure 6. (a) Comparison between hourly observed (red dotted line) and simulated (blue dotted line) temperature at 2-m above ground (T2) averaged at 70 Taiwan EPA's meteorological stations from 22 to 31 March 2006. The average hourly values of the measurement stations in each grid cell were compared to the simulated values of the corresponding cell grids. Mean bias of T2 between the simulation and observation are calculated for the period of 22–28 March and 29–31 March, respectively. The maximum hourly bias for the last 3 days is highlighted in the figure. (b) The locations of weather stations used for model evaluation. MB = mean bias.

both strong climate forcers with high uncertainties (Myhre et al., 2013). The WRF model was applied to conduct a quasi-quantitative assessment of this effect. Figure 6 compares the time series of observed and simulated temperature at 2-me above ground (T2) in Taiwan during 22–31 March 2006. A total of 70 ground-based meteorological stations operated by Taiwan EPA were used against the WRF simulation results. As shown in Figure 6, observed T2 temperature averaged at all stations and the mean simulated temperature sampled at the same stations covaried relatively consistently at most time steps during 22–28 March. The mean bias (MB) of T2 (MB $= \frac{1}{N} \sum_{i=1}^{N} C_m - C_o$, where $C_{m,i}$ and $C_{o,i}$ denotes the simulated and observed T2 at site i, respectively) during 22–28 March was calculated to be −0.36 °C. This mean bias was well within the legislated benchmark value of ±0.5 °C (Emery et al., 2001), indicating the configuration of physical schemes used in the WRF model was representative of the investigated domain and could reasonably simulate the meteorological fields in terms of no significant intrusion of air pollutants. However, the simulation tended to deviate from the observations since 29 March, which was exactly the date when intensive plume intrusion occurred. T2 was significantly underestimated throughout 29–31 March, exhibiting larger discrepancies during daytime. For instance, the negative bias reached 3.20–3.85 °C during 3–8 UTC on 29 March, 3.12–3.42 °C during 3–7 UTC on 30 March, and 1.97–2.26 °C during 3–7 UTC on 31 March, respectively. Overall, the mean bias during 29–31 March reached −2.19°C, much larger than the benchmark, suggesting the incapability of WRF model reproducing T2 during this period. Since the model already demonstrated its reliability of simulating the meteorology before 29 March, it should not be the model configuration issues that induced this phenomenon. Hence, the likely reason was due to the influence of intruded aerosols on modifying the regional meteorology as WRF was purely run without accounting for the aerosol-meteorology feedback effect. It was also found that the simulated temperature was negatively biased more during daytime than nighttime. This further confirmed the aerosol-meteorology effect as heating of the atmosphere was more obvious under conditions of solar radiation.

4.1.2. Warming in the Upper Layer

In addition to the observational evidence of warming near the surface, we also analyzed the possible perturbation of this long-range transport event on the vertical profile of temperature. Meteorological sounding sites were selected mainly from Eastern and Southern China as shown in Figure 7. We compared the temperature profiles measured at various sites in mainland China to the modeled results on 0:00 UTC, 29
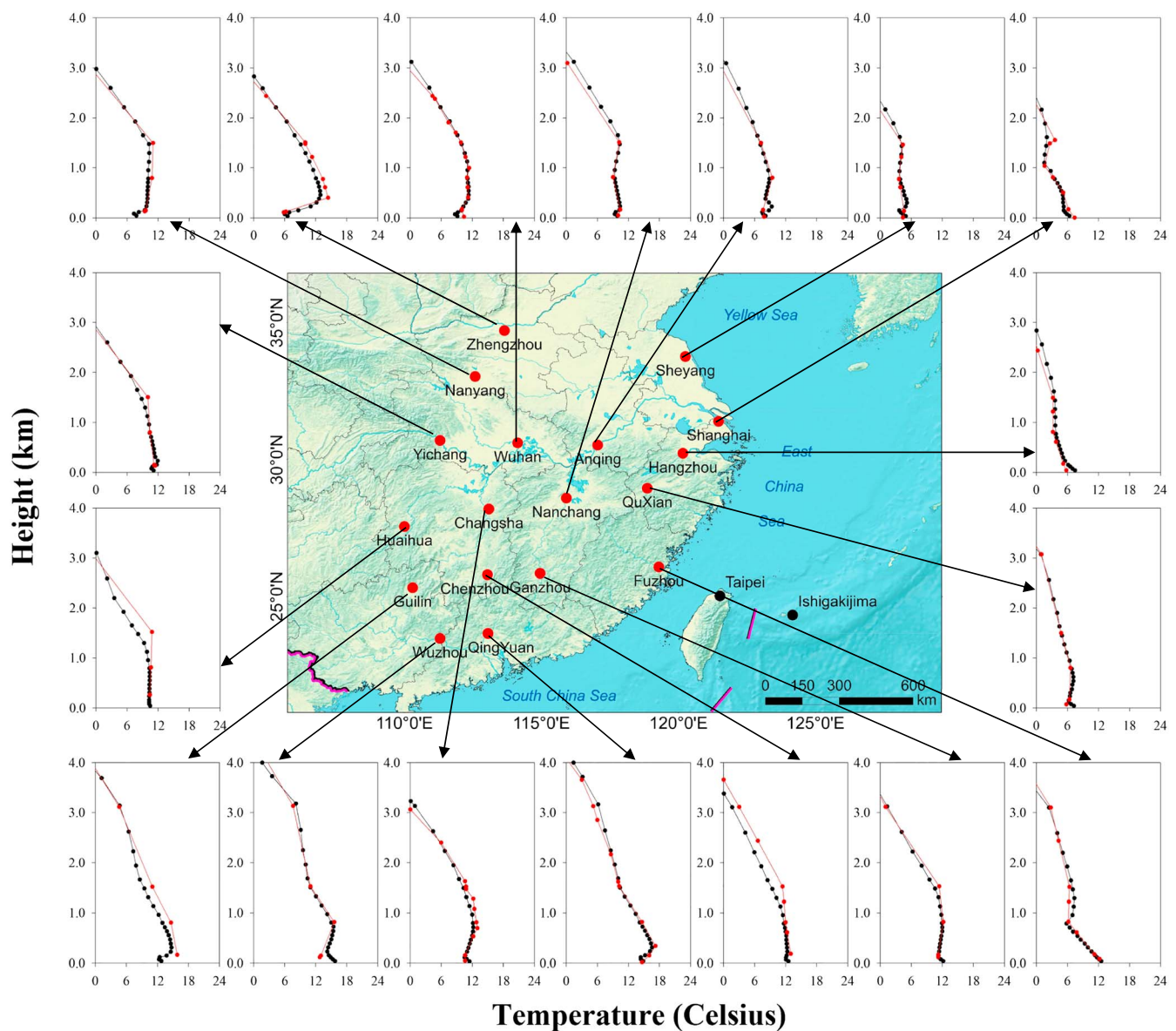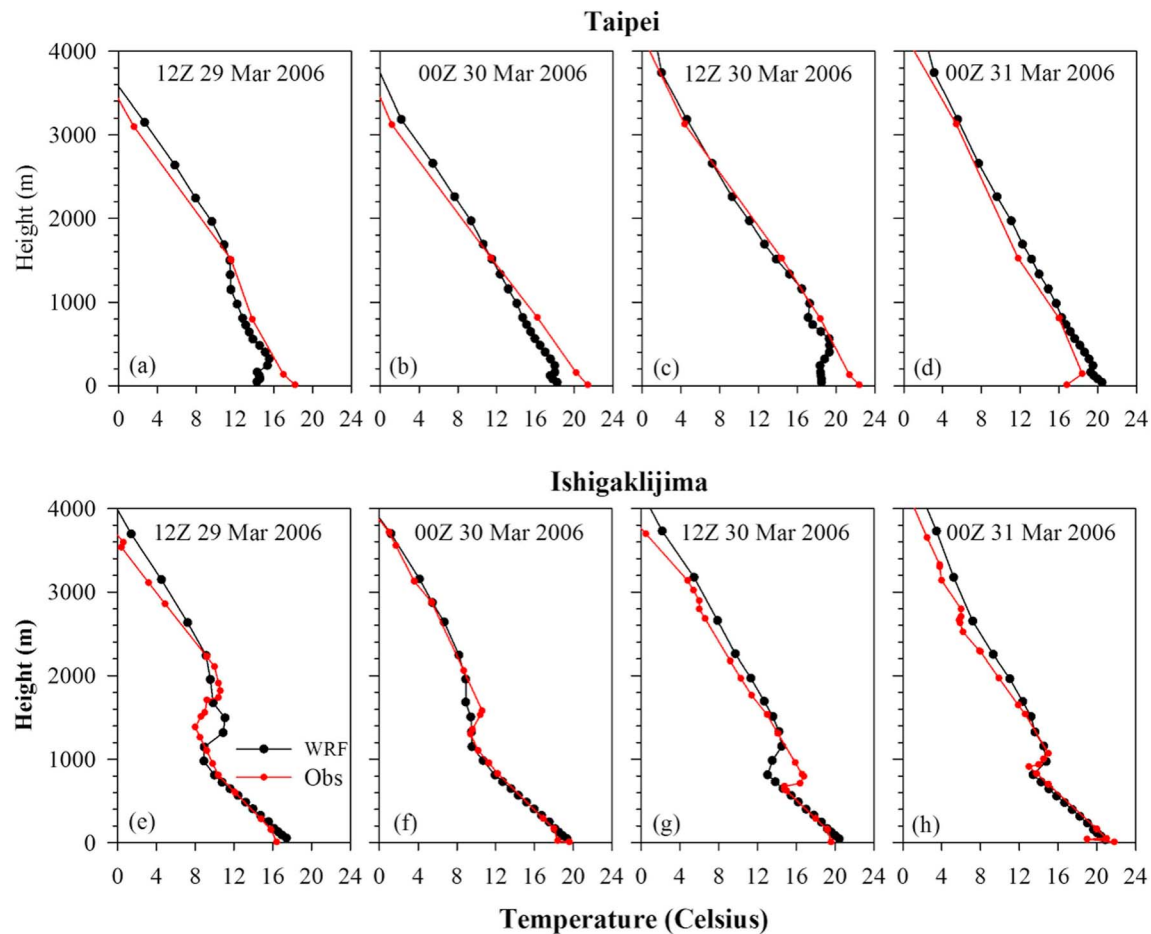
Figure 7. Comparison of temperature profiles (00UTC, 29 March 2006) between observation (red line) and WRF simulation (black line) at 18 sounding sites in Eastern and Southern China.

March when the particulate pollution was not so intense. Generally, the temperature profiles were relatively well reproduced by the WRF simulation in regard of the magnitudes and vertical structure although the deviation of modeled temperature from observation could be found at certain altitudes of various sounding sites. This could be ascribed to several factors. First, the spatial resolution of 36 km of the simulation may still be not fine enough for reproducing the site-based meteorology observation. On the other hand, the vertical resolutions of sounding data varied greatly among different sounding sites and were generally coarser compared to the simulation. The mismatch of the vertical resolution between observation and simulation also partly explained the modeled bias. Overall, we reinforced that the simulation was capable of reproducing the temperature profiles when the particulate pollution was not intense on 29 March.

As a comparison, the model simulation of temperature profiles at the Taipei-CWB site did not perform as well as the mainland sites (Figures 8a–8c). It was evident that the simulated temperature near the surface was much lower than the observation, yielding a negative bias of 4.0, 3.3, and 3.9 °C at 12:00, 29 March,

Figure 8. Comparison of temperature profiles between observation (red line) and WRF simulation (black line) at the Ishigaki-jima and Taipei sounding sites (locations shown in Figure 8) from 12 UTC, 29 March, to 00 UTC, 31 March 2006.

00:00, 30 March, and 12:00, 30 March, respectively. This was consistent with results in section 4.3.1 that warming near the surface was found. In addition, warming extending from near the surface to higher altitudes were also observed with different warming extents. At 00:00, 31 March (Figure 8d), when the aerosol plumes were intercepted by precipitation, no warming was observed at all altitudes.

We further compared the model and observation at another sounding site, Ishigaki-jima, which is about 270-km east of Taiwan (Figures 8e–8h and location shown in Figure 7). At 12:00, 29 March, the discrepancy between simulated and observed temperature mainly occurred between 1.1 and 2.2 km, exhibiting slight warming at around 1.7–2.2km. The warming was strengthened on the next two sounding dates. At 00:00, 30 March, the negative bias of simulated temperature mainly occurred at 1.4–1.9 km with the strongest value of $-1.6\,°C$ at around 1.6 km. At 12:00, 30 March, the vertical structure of the negative temperature bias moved to lower altitudes of around 0.7–1.1 km with the strongest warming of 3.4 °C at around 0.8 km. After 12 hr at 0:00, 31 March, no warming at all altitudes were observed As Ishigaki-jima is a remote island over the West Pacific with almost no anthropogenic emissions, the warming at the higher altitudes further demonstrated the perturbation of long-range transported aerosol on the local meteorology.

4.2. Radiative Forcing and Heating Rates Due to Transported Aerosol Plumes

A radiative transfer model CLIRAD (FC05)-SW was applied to estimate the radiative forcing and heating rates due to transported aerosol plumes. Since the Lidar measurement cannot retrieve the aerosol microphysical properties, the essential parameters (i.e., asymmetry factor and single scattering albedo) as inputs for the radiative transfer model were retrieved from the AERONET measurements. Due to the different
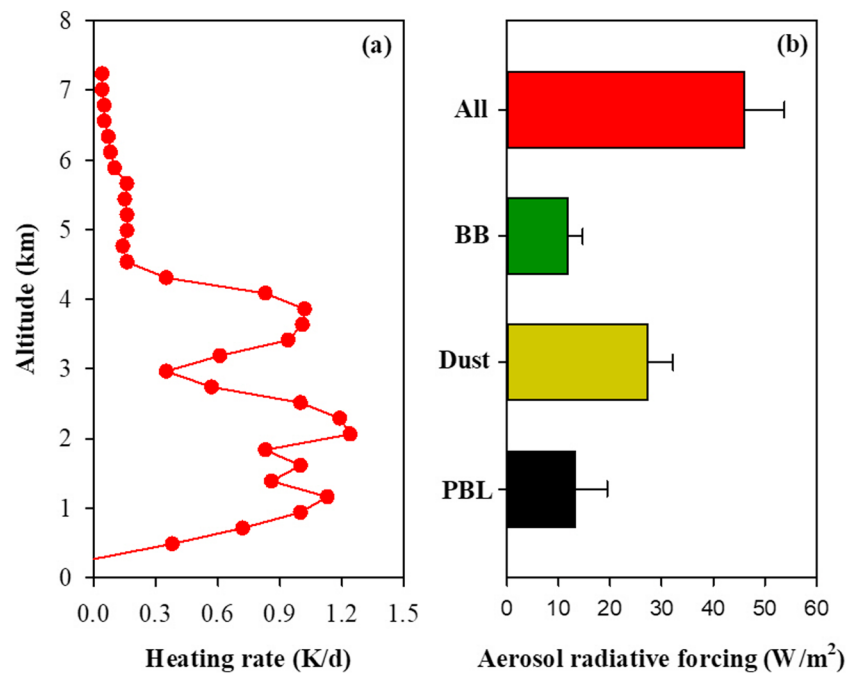
Figure 9. (a) Simulated average instantaneous heating rates due to the aerosol plumes between 06:59 and 8:57 UTC on 30 March. (b) Aerosol radiative forcing in the atmosphere due to the aerosol within the PBL layer, dust layer, biomass burning layer, and the whole column aerosols, respectively. Error bar represents one standard deviation.

characteristics of aerosols at various altitudes, a columnar constant profile of aerosol microphysical parameters should not be used. Instead, the aerosol microphysical parameters dependent on altitudes were desired. In this regard, the whole extinction profiles were grouped into three categories as similar as in section 3.2.3. The aerosol microphysical properties near the surface within the boundary layer were based on a slightly polluted day (11 March 2006, τ_{500} =0.44) at the Taipei_CWB site. The aerosol microphysical properties of the dust layer were based on the measurement at the Taihu AERONET site on 28 March, when the dust transported from northern China was intense as discussed in section 3.2.1. The aerosol microphysical properties of the biomass burning layer were based on the measurement on 30 March at the Lulin AERONET site, which was found almost exclusively impacted by the biomass burning plume. Based on the interpolation method in section 2.3, the values of single scattering albedo and asymmetry factor at eight wavelengths for the three aerosol categories are derived and presented in Table S1.

Figure 9a shows the instantaneous heating rates based on the aerosol extinction profiles measured by the MPL Lidar at 06:59–08:57 UTC, 30 March and the presumed aerosol microphysical properties. Generally, the vertical profile of aerosol heating rates varied as similar as its extinction profiles. The instantaneous heating rate increased quickly from near the surface to 0.72 K/day at the altitude of around 700 m. Within the dust layer at around 0.7–2.6 km, the heating rates fluctuated within 0.83–1.24K/day with an average of 1.04K/day. Above the dust layer, the heating rates increased from 0.35 K/day at around 3 km to a peak value of 1.02 K/day at 3.9 km and then quickly decreased till almost zero above 6 km. The peak values of heating rates in this episode were at the similar magnitudes of that of black carbon aerosols during a haze episode in Eastern China (Li et al., 2015). The vertical structure of aerosol heating rates clearly exhibited multiple layers of atmospheric heating due to the intruded aerosol plumes. Such high atmospheric heating at multiple altitude levels would surely result in strengthening of the inversion layer, leading to poor dispersal of aerosols and thus providing a positive feedback between meteorology and aerosols.

Aerosol radiative forcing in the atmosphere are shown in Figure 9b. In addition to the overall radiative forcing from the whole columnar aerosols, sensitivity simulations of the aerosol radiative forcing were conducted by assuming that only near surface, dust, or biomass burning aerosols existed. It was calculated that the radiative forcing of the near surface, dust, and biomass burning aerosols in the atmosphere were
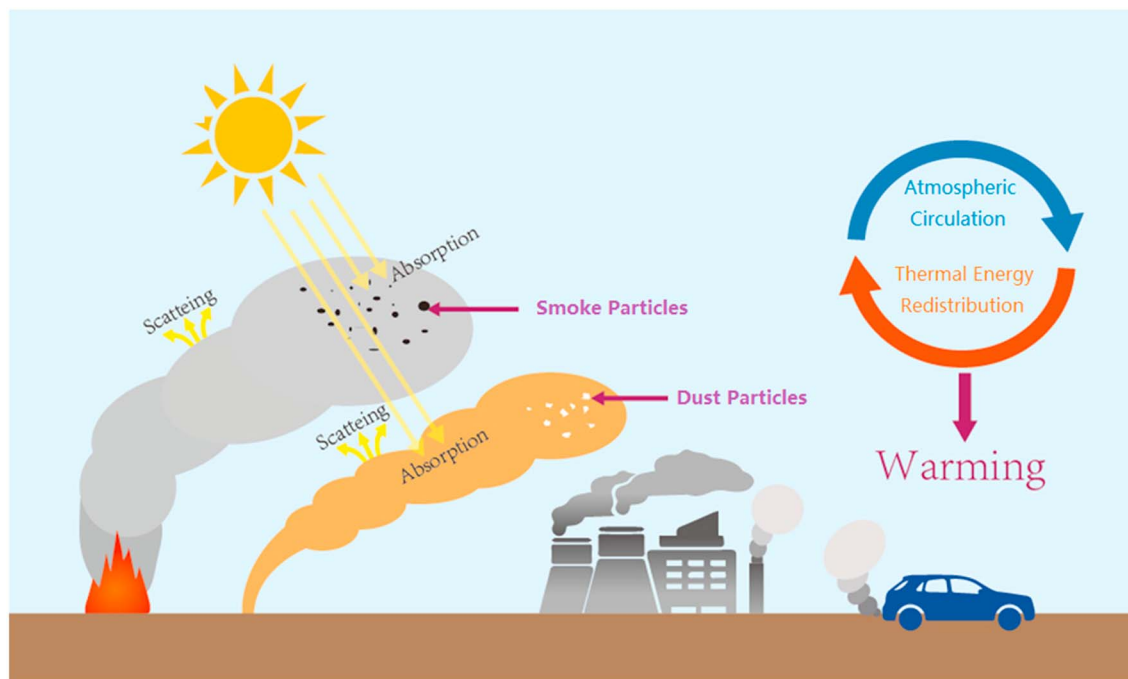
Figure 10. The conceptual model for the "double dome" warming effect mechanism.

13.2, 27.3, and 11.9 W/m^2, respectively. As a comparison, the radiative forcing of the whole columnar aerosols reached 46.0 W/m^2, suggesting almost an aggregating heating effect from the multilayered aerosols.

4.3. Implications

A simple conceptual model is established based on this specific case study (Figure 10). The assumptions explaining this phenomenon are as follows. When the two types of absorbing aerosols (i.e., biomass burning and dust aerosols) are present and reside above the boundary layer, it is likely that the backscattered sunlight by the aerosols within PBL could have been partially absorbed by the absorbing aerosols at the higher altitudes. The biomass burning plume in the upper layer and dust in the middle layer seem to act as a "double dome" constraining the thermal radiation. Given the enhanced atmospheric circulation and mixing processes in the lower troposphere due to the heating of the upper levels as a "heat pump" (Gong et al., 2007), the thermal energy could be redistributed and warm the surface. This partially explain the phenomenon that strong warming near the surface occurred due to the intrusion of biomass burning and dust aerosols in the high altitudes. However, to prove this assumption, more detailed characterization of the vertical profiles of aerosol chemical components, mixing state, and microphysical optical properties is required. Moreover, advanced aerosol-meteorology feedback module is essential for quantifying the aerosol radiative forcing and temperature response.

5. Conclusions

On 29–31 March 2006, one MicroPulse Lidar set up in Taiwan observed a continuous long-range transport event with multiple aerosol layers. The upper and middle aerosol layers decoupled in the beginning of the event with a duration of about 18 hr. Afterward, the middle aerosol layer gradually merged into the boundary layer. Backward trajectories were computed at three levels of 0.8, 1.9, and 3.5 km, corresponding to the altitudes of the multiple observed aerosol extinction peaks. It was found that the backward trajectories at the lower and middle altitudes of 0.8 and 1.9 km both traced back to the arid and semi-arid regions in inner-Mongolia of China and Mongolia where the Gobi Desert is located, while the backward trajectories at the high-altitude (above 3 km) originated from Southeast Asia where biomass burning activities were most intense in spring.

The aerosol microphysical optical properties were investigated at multiple AERONET sites. On the dust transport pathway, aerosol optical depth maintained at high levels but with elevated Ångström exponent, suggesting enhanced mixing extent of dust and anthropogenic pollutants. One near sea level and one high mountain AERONET site differentiated the characteristics of aerosols from different sources. The near sea level site showed high AOD but low values of Ångström exponent. Coarse particles contributed a significant fraction of 39% to AOD, indicating strong impact from the mineral dust. In contrast, the high mountain site (elevation of ~3 km) exhibited moderate AOD but high values of Ångström exponent as well as low contribution from coarse AOD of about 10%, suggesting the dominance of biomass burning aerosols but negligible impact from dust.

Regional meteorology was simulated by WRF and evaluated against a Taiwan-wide surface meteorology network and sounding data at multiple sites. As for the weeklong period before this long-range transport event, temperature was well simulated within the model evaluation benchmark of less than 0.5 °C. However, the simulated temperature was biased low of more than 2 °C during the event, which in turn meant strong warming near the surface due to the intrusion of aerosol plumes. We proposed a warming effect mechanism so-called double dome. The biomass burning and dust aerosol plumes above the boundary layer served like two curtains by reserving the radiation reflected by the near surface aerosols. After the atmospheric circulation and heat redistribution, the near ground surface could be warmed to some extent. This study elucidated that the intensive long-range transport of particulate matters can significantly modify the regional/local meteorology of the receptor area.

To further assess the radiative effects at a larger geographic scale, a chemical transport modeling with the chemistry-meteorology two-way feedback is desired. However, due to the highly uncertain dust and biomass burning emissions (Dong et al., 2016; Fu et al., 2012) as well as inadequate dust heterogeneous chemistry (e.g., in the Community Multiscale Air Quality model, Dong et al., 2016), credible simulation results of radiative effects for this special case were not expected. Hence, in this case study, we conducted the numerical simulation without aerosol feedback and direct comparison with observation, which should be more accurate in quantifying the aerosol-meteorology effects.

References

Arimoto, R., Balsam, W., & Schloesslin, C. (2002). Visible spectroscopy of aerosol particles collected on filters: Iron-oxide minerals. *Atmospheric Environment*, *36*(1), 89–96. https://doi.org/10.1016/S1352-2310(01)00465-4

Bauer, S., Bierwirth, E., Esselborn, M., Petzold, A., Macke, A., Trautmann, T., & Wendisch, M. (2011). Airborne spectral radiation measurements to derive solar radiative forcing of Saharan dust mixed with biomass burning smoke particles. *Tellus B: Chemical and Physical Meteorology*, *63*(4), 742–750. https://doi.org/10.1111/j.1600-0889.2011.00567.x

Campbell, J. R., Welton, E. J., Spinhirne, J. D., Ji, Q., Tsay, S. C., Piketh, J. S., et al. (2002). Full-time, eye-safe cloud and aerosol lidar observation at atmospheric radiation measurement program sites: Instruments and data processing. *Journal of Atmospheric & Oceanic Technology*, *19*(4), 431–442. https://doi.org/10.1175/1520-0426(2002)019<0431:FTESCA>2.0.CO;2

Campbell, J. R., Welton, E. J., Spinhirne, J. D., Ji, Q., Tsay, S.-C., Piketh, S. J., et al. (2003). Micropulse lidar observations of tropospheric aerosols over northeastern South Africa during the ARREX and SAFARI 2000 dry season experiments. *Journal of Geophysical Research*, *108*(D13), 8497. https://doi.org/10.1029/2002JD002563

Chang, S. C., Chou, C. C., Chen, W. N., & Lee, C. T. (2010). Asian dust and pollution transport—A comprehensive observation in the downwind Taiwan in 2006. *Atmospheric Research*, *95*(1), 19–31. https://doi.org/10.1016/j.atmosres.2009.07.012

Chen, W. N., Tsai, F. J., Chou, C. C. K., Chang, S. Y., Chen, Y. W., & Chen, J. P. (2007). Optical. properties of Asian dusts in the free atmosphere measured by Raman lidar at Taipei, Taiwan. *Atmospheric Environment*, *41*(36), 7698–7714. https://doi.org/10.1016/j.atmosenv.2007.06.001

Chou, M. D., Chan, P. K., & Wang, M. (2002). Aerosol radiative forcing derived from SeaWIFS-Retrieved aerosol optical properties. *Journal of the Atmospheric Sciences*, *59*(3), 748–757. https://doi.org/10.1175/1520-0469(2002)059<0748:ARFDFS>2.0.CO;2

Chou, M. D., & Suarez, M. J. (1999). A shortwave radiation parameterization for atmospheric studies, in Technical Report Series on Global Modeling and Data Assimilation, 15, NASA/TM-1999-104606. 40 pp.

Chuang, M. T., Fu, J. S., Jang, C. J., Chan, C. C., Ni, P. C., & Lee, C. T. (2008). Simulation of a long-range transport aerosols from the Asian continent to Taiwan by a southward Asian high-pressure system. *Science of the Total Environment*, *406*(1-2), 168–179. https://doi.org/10.1016/j.scitotenv.2008.07.003

Deaton, B. C., & Balsam, W. L. (1991). Visible spectroscopy—A rapid method for determining hematite and goethite concentration in geological-materials. *Journal of Sedimentary Petrology*, *61*(4), 628–632. https://doi.org/10.1306/D4267794-2B26-11D7-8648000102C1865D

Ding, A. J., Fu, C. B., Yang, X. Q., Sun, J. N., Petäjä, T., Kerminen, V. M., et al. (2013). Intense atmospheric pollution modifies weather: A case of mixed biomass burning with fossil fuel combustion pollution in eastern China. *Atmospheric Chemistry and Physics*, *13*(20), 10,545–10,554. https://doi.org/10.5194/acp-13-10545-2013

Dong, X., Fu, J. S., Huang, K., Tong, D., & Zhuang, G. (2016). Model development of dust emission and heterogeneous chemistry within the Community Multiscale Air Quality modeling system and its application over East Asia. *Atmospheric Chemistry and Physics*, *16*, 8157–8180. https://doi.org/10.5194/acp-16-8157-2016

Draxier, R. R., & Hess, G. D. (1998). An overview of the HYSPLIT_4 modelling system for trajectories, dispersion and deposition. *Australian Meteorological Magazine*, *47*(4), 295–308.

Draxler, R. R., & Rolph, G. D. (2015). HYSPLIT (HYbrid Single-Particle Lagrangian Integrated Trajectory) Model access via NOAA ARL READY Website (http://ready.arl.noaa.gov/HYSPLIT.php). NOAA Air Resources Laboratory, Silver Spring, MD.

Dubovik, O., Holben, B., Eck, T. F., Smirnov, A., Kaufman, Y. J., King, M. D., et al. (2002). Variability of absorption and optical properties of key aerosol types observed in worldwide locations. *Journal of the Atmospheric Sciences*, *59*(3), 590–608. https://doi.org/10.1175/1520-0469(2002)059<0590:VOAAOP>2.0.CO;2

Eck, T. F., Holben, B. N., Reid, J. S., Dubovik, O., Smirnov, A., O'Neill, N. T., et al. (1999). Wavelength dependence of the optical depth of biomass burning, urban, and desert dust aerosols. *Journal of Geophysical Research*, *104*(D24), 31,333–31,349. https://doi.org/10.1029/1999JD900923

Emery, C., Tai, E., & Yarwood, G. (2001). Enhanced meteorological modeling and performance evaluation for two Texas episodes. Report to the Texas Natural Resources Conservation Commission ENVIRON, International Corp Novato, CA, 2001.

Fomin, B. A., & Correa, M. P. (2005). A k-distribution technique for radiative transfer simulation in inhomogeneous atmosphere: 2. FKDM, fast k-distribution model for the shortwave. *Journal of Geophysical Research*, *110*, D02106. https://doi.org/10.01029/02004JD005163

Foyo-Moreno, I., Alados, I., Guerrero-Rascado, J. L., Lyamani, H., Pérez-Ramírez, D., Olmo, F. J., & Alados-Arboledas, L. (2019). Contribution to column integrated aerosol typing based on Sun photometry using different criteria. *Atmospheric Research*, *224*, 1–17. https://doi.org/10.1016/j.atmosres.2019.03.007

Fu, J. S., Hsu, N. C., Gao, Y., Huang, K., Li, C., Lin, N. H., & Tsay, S. C. (2012). Evaluating the influences of biomass burning during 2006 BASE-ASIA: A regional chemical transport modeling. *Atmospheric Chemistry and Physics*, *12*(9), 3837–3855. https://doi.org/10.5194/acp-12-3837-2012

Giles, D. M., Holben, B. N., Eck, T. F., Sinyuk, A., Smirnov, A., Slutsker, I., et al. (2012). An analysis of AERONET aerosol absorption properties and classifications representative of aerosol source regions. *Journal of Geophysical Research*, *117*, D17203. https://doi.org/10.1029/2012JD018127

Gong, D.-Y., Ho, C.-H., Chen, D., Qian, Y., Choi, Y.-S., & Kim, J. (2007). Weekly cycle of aerosol-meteorology interaction over China. *Journal of Geophysical Research*, *112*, D22202. https://doi.org/10.1029/2007JD008888

Groß, S., Tesche, M., Freudenthaler, V., Toledano, C., Wiegner, M., Ansmann, A., et al. (2011). Characterization of Saharan dust, marine aerosols and mixtures of biomass-burning aerosols and dust by means of multi-wavelength depolarization and Raman lidar measurements during SAMUM 2. *Tellus B: Chemical and Physical Meteorology*, *63*(4), 706–724. https://doi.org/10.1111/j.1600-0889.2011.00556.x

Hand, V. L., Capes, G., Vaughan, D. J., Formenti, P., Haywood, J. M., & Coe, H. (2010). Evidence of internal mixing of African dust and biomass burning particles by individual particle analysis using electron beam techniques. *Journal of Geophysical Research*, *115*, D13301. https://doi.org/10.1029/2009JD012938

Holben, B. N., Eck, T. F., Slutsker, I., Tanré, D., Buis, J. P., Setzer, A., et al. (1998). AERONET—A federated instrument network and data archive for aerosol characterization. *Remote Sensing of Environment*, *66*(1), 1–16. https://doi.org/10.1016/S0034-4257(98)00031-5

Huang, K., Fu, J. S., Christina Hsu, N., Gao, Y., Dong, X., Tsay, S.-C., & Lam, Y. F. (2013). Impact assessment of biomass burning on air quality in Southeast and East Asia during BASE-ASIA. *Atmospheric Environment*, *78*, 291–302. https://doi.org/10.1016/j.atmosenv.2012.03.048

Huang, K., Zhuang, G., Lin, Y., Fu, J. S., Wang, Q., Liu, T., et al. (2012). Typical types and formation mechanisms of haze in an Eastern Asia megacity, Shanghai. *Atmospheric Chemistry and Physics*, *12*(1), 105–124. https://doi.org/10.5194/acp-12-105-2012

Huang, K., Zhuang, G. S., Li, J. A., Wang, Q. Z., Sun, Y. L., Lin, Y. F., & Fu, J. S. (2010). Mixing of Asian dust with pollution aerosol and the transformation of aerosol components during the dust storm over China in spring 2007. *Journal of Geophysical Research*, *115*, D00K13. https://doi.org/10.1029/2009jd013145

Huang, K., Zhuang, G. S., Lin, Y. F., Li, J. A., Sun, Y. L., Zhang, W. J., & Fu, J. S. (2010). Relation between optical and chemical properties of dust aerosol over Beijing, China. *Journal of Geophysical Research*, *115*, D00K16. https://doi.org/10.1029/2009jd013212

Kanitz, T., Ansmann, A., Seifert, P., Engelmann, R., Kalisch, J., & Althausen, D. (2013). Radiative effect of aerosols above the northern and southern Atlantic Ocean as determined from shipborne lidar observations. *Journal of Geophysical Research: Atmospheres*, *118*, 12,556–12,565. https://doi.org/10.1002/2013JD019750

Keil, A., & Haywood, J. M. (2003). Solar radiative forcing by biomass burning aerosol particles during SAFARI 2000: A case study based on measured aerosol and cloud properties. *Journal of Geophysical Research*, *108*(D13), 8467. https://doi.org/10.1029/2002JD002315

Kim, S. W., Yoon, S. C., & Kim, J. (2008). Columnar Asian dust particle properties observed by sun/sky radiometers from 2000 to 2006 in Korea. *Atmospheric Environment*, *42*(3), 492–504. https://doi.org/10.1016/j.atmosenv.2007.09.055

Lee, C. T., Chuang, M. T., Lin, N. H., Wang, J. L., Sheu, G. R., Wang, S. H., et al. (2011). The enhancement of biosmoke from Southeast Asia on PM2.5 water-soluble ions during the transport over the Mountain Lulin site in Taiwan. *Atmospheric Environment*, *45*(32), 5784–5794. https://doi.org/10.1016/j.atmosenv.2011.07.020

Li, J., Fu, Q., Huo, J., Wang, D., Yang, W., Bian, Q., et al. (2015). Tethered balloon-based black carbon profiles within the lower troposphere of Shanghai in the 2013 East China smog. *Atmospheric Environment*, *123*, 327–338. https://doi.org/10.1016/j.atmosenv.2015.08.096

Lin, N. H., Tsay, S. C., Maring, H. B., Yen, M. C., Sheu, G. R., Wang, S. H., et al. (2013). An overview of regional experiments on biomass burning aerosols and related pollutants in Southeast Asia: From BASE-ASIA and the Dongsha Experiment to 7-SEAS. *Atmospheric Environment*, *78*, 1–19. https://doi.org/10.1016/j.atmosenv.2013.04.066

Loría-Salazar, S. M., Arnott, W. P., & Moosmüller, H. (2014). Accuracy of near-surface aerosol extinction determined from columnar aerosol optical depth measurements in Reno, NV, USA. *Journal of Geophysical Research: Atmospheres*, *119*, 11,355–311,374. https://doi.org/10.1002/2014JD022138

Mahowald, N. M., & Kiehl, L. M. (2003). Mineral aerosol and cloud interactions. *Geophysical Research Letters*, *30*(9), 1475. https://doi.org/10.1029/2002GL016762

Mardi, A. H., Dadashazar, H., MacDonald, A. B., Braun, R. A., Crosbie, E., Xian, P., et al. (2018). Biomass burning plumes in the vicinity of the California coast: Airborne characterization of physicochemical properties, heating rates, and spatiotemporal features. *Journal of Geophysical Research: Atmospheres*, *123*, 13,560–13,582. https://doi.org/10.1029/2018JD029134

Myhre, G., Shindell, D., Bréon, F.-M., Collins, W., Fuglestvedt, J., Huang, J., et al. (2013). Anthropogenic and natural radiative forcing. In T. F. Stocker, D. Qin, G.-K. Plattner, M. Tignor, S. K. Allen, J. Doschung, A. Nauels, Y. Xia, V. Bex, & P. M. Midgley (Eds.), *Climate Change 2013: The Physical Science Basis. Contribution of Working Group I to the Fifth Assessment Report of the Intergovernmental Panel on Climate Change* (pp. 659–740). Cambridge University Press. https://doi.org/10.1017/CBO9781107415324.018

Nguyen, D. L., Kim, J. Y., Ghim, Y. S., & Shim, S.-G. (2015). Influence of regional biomass burning on the highly elevated organic carbon concentrations observed at Gosan, South Korea during a strong Asian dust period. *Environmental Science and Pollution Research*, *22*(5), 3594–3605. https://doi.org/10.1007/s11356-014-3587-z

Noh, Y. M., Kim, Y. J., Choi, B. C., & Murayama, T. (2007). Aerosol lidar ratio characteristics measured by a multi-wavelength Raman lidar system at Anmyeon Island, Korea. *Atmospheric Research*, *86*, 76–87.

Noh, Y. M., Muller, D., Lee, H., Lee, K., Kim, K., Shin, S., & Kim, Y. J. (2012). Estimation of radiative forcing by the dust and non-dust content in mixed East Asian pollution plumes on the basis of depolarization ratios measured with lidar. *Atmospheric Environment*, *61*, 221–231. https://doi.org/10.1016/j.atmosenv.2012.07.034

Osborne, M., Malavelle, F. F., Adam, M., Buxmann, J., Sugier, J., Marenco, F., & Haywood, J. (2019). Saharan dust and biomass burning aerosols during ex-hurricane Ophelia: observations from the new UK lidar and sun-photometer network. *Atmospheric Chemistry and Physics*, *19*, 3557–3578.

Pan, X., Uno, I., Zhe, W., Nishizawa, T., Sugimoto, N., Yamamoto, S., et al. (2017). Real-time observational evidence of changing Asian dust morphology with the mixing of heavy anthropogenic pollution. *Science Report*, *7*, 335. https://doi.org/10.1038/s41598-017-00444-w

Pani, S. K., Wang, S. H., Lin, N. H., Lee, C. T., Tsay, S. C., Holben, B. N., et al. (2016). Radiative effect of springtime biomass-burning aerosols over Northern Indochina during 7-SEAS/BASELInE 2013 campaign. *Aerosol and Air Quality Research*, *16*(11), 2802–2817. https://doi.org/10.4209/aaqr.2016.03.0130

Pani, S. K., Wang, S. H., Lin, N. H., Tsay, S. C., Lolli, S., Chuang, M. T., et al. (2016). Assessment of aerosol optical property and radiative effect for the layer decoupling cases over the northern South China Sea during the 7-SEAS/Dongsha Experiment. *Journal of Geophysical Research: Atmospheres*, *121*, 4894–4906. https://doi.org/10.1002/2015JD024601

Papayannis, A., Zhang, H. Q., Amiridis, V., Ju, H. B., Chourdakis, G., Georgoussis, G., et al. (2007). Extraordinary dust event over Beijing, China, during April 2006: Lidar, Sun photometric, satellite observations and model validation. *Geophysical Research Letters*, *34*, L07806. https://doi.org/10.1029/2006gl029125

Reid, J. S., Hyer, E. J., Prins, E. M., Westphal, D. L., Zhang, J., Wang, J., et al. (2009). Global monitoring and forecasting of biomass-burning smoke: Description of and lessons from the Fire Locating and Modeling of Burning Emissions (FLAMBE) Program. *IEEE J-Stars*, *2*(3), 144–162. https://doi.org/10.1109/Jstars.2009.2027443

Rittmeister, F., Ansmann, A., Engelmann, R., Skupin, A., Baars, H., Kanitz, T., & Kinne, S. (2017). Profiling of Saharan dust from the Caribbean to western Africa - Part 1: Layering structures and optical properties from shipborne polarization/Raman lidar observations. *Atmospheric Chemistry and Physics*, *17*, 12,963–12,983.

Sheu, G. R., Lin, N. H., Wang, J. L., Lee, C. T., Yang, C. F. O., & Wang, S. H. (2010). Temporal distribution and potential sources of atmospheric mercury measured at a high-elevation background station in Taiwan. *Atmospheric Environment*, *44*(20), 2393–2400. https://doi.org/10.1016/j.atmosenv.2010.04.009

Sicard, M., Mallet, M., García-Vizcaíno, D., Comerón, A., Rocadenbosch, F., Dubuisson, P., & Muñoz-Porcar, C. (2012). Intense dust and extremely fresh biomass burning outbreak in Barcelona, Spain: Characterization of their optical properties and estimation of their direct radiative forcing. *Environmental Research Letters*, *7*(3). https://doi.org/10.1088/1748-9326/7/3/034016

Tesche, M., Gross, S., Ansmann, A., Müller, D., Althausen, D., Freudenthaler, V., & Esselborn, M. (2011). Profiling of Saharan dust and biomass-burning smoke with multiwavelength polarization Ramanlidar at Cape Verde. *Tellus B: Chemical and Physical Meteorology*, *63*(4), 649–676. https://doi.org/10.1111/j.1600-0889.2011.00548.x

Tian, P., Zhang, L., Cao, X., Sun, N., & Wang, H. (2018). Enhanced bottom-of-the-atmosphere coolingand atmosphere heating efficiency by mixedtype aerosols: a classification based on aerosol nonsphericity. *Journal of the Atmospheric Sciences*, *75*(1),113–124.

Tian, P., Zhang, L., Ma, J., Tang, K., Xu, L., Wang, Y., et al. (2018). Radiative absorption enhancement of dust mixed with anthropogenic pollution over East Asia. *Atmospheric Chemistry and Physics*, *18*, 7815–7825. https://doi.org/10.5194/acp-18-7815-2018

Tobo, Y., Zhang, D. Z., Matsuki, A., & Iwasaka, Y. (2010). Asian dust particles converted into aqueous droplets under remote marine atmospheric conditions. *Proceedings of the National Academy of Sciences of the United States of America*, *107*(42), 17,905–17,910. https://doi.org/10.1073/pnas.1008235107

Torres, O., Tanskanen, A., Veihelmann, B., Ahn, C., Braak, R., Bhartia, P. K., et al. (2007). Aerosols and surface UV products from Ozone Monitoring Instrument observations: An overview. *Journal of Geophysical Research*, *112*, D24S47. https://doi.org/10.1029/2007jd008809

Tsai, F., Chen, G. T. J., Liu, T. H., Lin, W. D., & Tu, J. Y. (2008). Characterizing the transport pathways of Asian dust. *Journal of Geophysical Research*, *113*, D17311. https://doi.org/10.1029/2007jd009674

Tsay, S. C., Hsu, N. C., Lau, W. K. M., Li, C., Gabriel, P. M., Ji, Q., et al. (2013). From BASE-ASIA toward 7-SEAS: A satellite-surface perspective of boreal spring biomass-burning aerosols and clouds in Southeast Asia. *Atmospheric Environment*, *78*, 20–34. https://doi.org/10.1016/j.atmosenv.2012.12.013

Wang, Q., Dong, X., Fu, J. S., Xu, J., Deng, C., Jiang, Y., et al. (2018). Environmentally dependent dust chemistry of a super Asian dust storm in March 2010: Observation and simulation. *Atmospheric Chemistry and Physics*, *18*(5), 3505–3521. https://doi.org/10.5194/acp-18-3505-2018

Wang, S. H., Lin, N. H., Chou, M. D., Tsay, S. C., Welton, E. J., Hsu, N. C., et al. (2010). Profiling transboundary aerosols over Taiwan and assessing their radiative effects. *Journal of Geophysical Research*, *115*, D00K31. https://doi.org/10.1029/2009jd013798

Wang, S.-H., Lin, N.-H., Chou, M.-D., & Woo, J.-H. (2007). Estimate of radiative forcing of Asian biomass-burning aerosols during the period of TRACE-P. *Journal of Geophysical Research*, *112*, D10222. https://doi.org/10.1029/2006JD007564

Wang, S. H., Lin, N. H., Kuo, C., Huang, Z., Holben, B. N., & Tsay, S. C. (2014). Long-term measurements of solar radiation and aerosol optical depth at Mt. Lulin (2,862 m) in East Asia, 2014 NOAA ESRL GLOBAL MONITORING ANNUAL CONFERENCE, Boulder, Colorado.

Wang, W., Ma, J. Z., Hatakeyama, S., Liu, X. Y., Chen, Y., Takami, A., et al. (2008). Aircraft measurements of vertical ultrafine particles profiles over Northern China coastal areas during dust storms in 2006. *Atmospheric Environment*, *42*(22), 5715–5720. https://doi.org/10.1016/j.atmosenv.2008.03.042

Wang, Y., Zhuang, G. S., Sun, Y., & An, Z. S. (2005). Water-soluble part of the aerosol in the dust storm season—Evidence of the mixing between mineral and pollution aerosols. *Atmospheric Environment*, *39*(37), 7020–7029. https://doi.org/10.1016/j.atmosenv.2005.08.005

Weinzierl, B., Sauer, D., Esselborn, M., Petzold, A., Veira, A., Rose, M., et al. (2011). Microphysical and optical properties of dust and tropical biomass burning aerosol layers in the Cape Verde region-an overview of the airborne in situ and lidar measurements during SAMUM-2. *Tellus B: Chemical and Physical Meteorology*, *63*(4), 589–618. https://doi.org/10.1111/j.1600-0889.2011.00566.x

Welton, E. J., Voss, K. J., Quinn, P. K., Flatau, P. J., Markowicz, K., Campbell, J. R., et al. (2002). Measurements of aerosol vertical profiles and optical properties during INDOEX 1999 using micropulse lidars. *Journal of Geophysical Research*, *107*(D19), 8019. https://doi.org/10.1029/2000JD000038

Won, J.-G., Yoon, S.-C., Kim, S.-W., Jefferson, A., Dutton, E. G., & Holben, B. N. (2004). Estimation of direct radiative forcing of Asian dust aerosols with sun/sky radiometer and lidar measurements at Gosan, Korea. *Journal of the Meteorological Society of Japan Ser. II*, *82*(1), 115–130. https://doi.org/10.2151/jmsj.82.115

Yen, M.-C., Peng, C.-M., Chen, T.-C., Chen, C.-S., Lin, N.-H., Tzeng, R.-Y., et al. (2013). Climate and weather characteristics in association with the active fires in northern Southeast Asia and spring air pollution in Taiwan during 2010 7-SEAS/Dongsha Experiment. *Atmospheric Environment*, *78*, 35–50. https://doi.org/10.1016/j.atmosenv.2012.11.015

Zhang, Y., Fu, R., Yu, H., Qian, Y., Dickinson, R., Silva Dias, M. A. F., et al. (2009). Impact of biomass burning aerosol on the monsoon circulation transition over Amazonia. *Geophysical Research Letters*, *36*, L10814. https://doi.org/10.1029/2009GL037180